Separation and Purification Technology 320 (2023) 124140

Contents lists available at ScienceDirect

Separation and Purification Technology

journal homepage: www.elsevier.com/locate/seppur

Magnetically recoverable Fe_3O_4/MoS_2/BiOI microspheres for visible light water disinfection: Molecular mechanism and transcriptomic insights

Yijun Shi [a], Jiaxin Ma [a], David Hanigan [b], Yanan Chen [a], Yunkun Qian [a], Jun Guo [a], Dong An [a,c,*]

[a] Department of Environmental Science & Engineering, Fudan University, Shanghai 200438, PR China
[b] Department of Civil and Environmental Engineering, University of Nevada, Reno, NV 89557-0258, USA
[c] Shanghai Institute of Pollution Control and Ecological Security, Shanghai 200092, PR China

ARTICLE INFO

Keywords:
Visible light
Subcellular damage
Water disinfection
Photocatalysis
Transcriptome

ABSTRACT

Photocatalysis driven by green energy is ideal for water purification. To gain a deeper understanding of the underlying mechanism behind the photocatalytic inactivation of bacteria, a novel visible-light-driven Fe_3O_4/MoS_2/BiOI (FMB) photocatalyst was synthesized, and *E. coli* disinfection was demonstrated. Complete inactivation of *E. coli* was achieved in 100 min by FMB exposed to 30 mW/cm^2 of > 400 nm light. FMB can also effectively reduce the total number of bacteria and heterotrophic bacteria in actual source water. The photochemical experiments revealed that h^+, e^-, H_2O_2, $^1O_2$ and $\bullet O_2^-$ were responsible for inactivation reactions. The semipermeable membrane experiments provided further evidence that contact between the photocatalyst and the bacteria was necessary to achieve inactivation. During the disinfection process, the zeta potential of the cells first decreased and then increased, while the particle size first increased and then decreased, indicating the rupture of the cells. Scanning electron microscopy, potassium ion leakage, and changes in cell surface hydrophobicity and hydrophilicity all confirmed the destruction of the *E. coli* cell membrane at the molecular level. The β-GAL activity of *E. coli* decreased, and the activities of superoxide dismutase (SOD) and catalase (CAT) increased initially, but subsequently decreased, further demonstrating disruption of the cell membrane and the leakage of cell contents. Transcriptomics was employed to understand gene expression and confirm bacterial membrane damage followed by oxidative stress response. This work provides a demonstration of the FMB inactivation by visible light and a mechanistic understanding of inactivation of *E. coli*.

1. Introduction

Bacterial contamination of drinking water supplies is a global issue [1,2] and contamination of drinking water by waterborne pathogenic microorganisms is widespread in countries at all levels of economic development. To prevent the spread of disease, safeguard human health, and simultaneously ensure clean access to water, disinfection of water must be conducted. Commonly used disinfection processes such as chlorination, ozonation and ultraviolet irradiation require expensive chemicals, can form unwanted disinfection by-products, and/or are energy intensive [3,4].

Photocatalysis technology generally produces singlet oxygen ($^1O_2$), superoxide radicals ($\bullet O_2^-$), hydroxyl radicals (•OH), electrons (e^-) and holes (h^+), all of which are highly reactive and can degrade organic matter or inactivate pathogens without producing toxic byproducts [5,6]. Compared to traditional catalysts (such as TiO_2) that can only be excited by ultraviolet light (4% of incident solar energy) [7,8], Bi-based photocatalyst is considered ideal materials for natural solar water disinfection due to their excellent optical properties [9–15]. Single- or several-layer MoS_2 nanoplates are relatively simple to produce and have a lower band gap (1.2 eV) [16], high specific surface area, and strong visible light adsorption [17]. Compared with pure BiOI and MoS_2, heterostructured MoS_2/BiOI (MB) has been shown to have increased photocatalytic activity because of its greater number of catalytic sites, faster photogenerated carrier transfer, and superior visible light absorption ability [18]. However, in practice, it is difficult to recover well-dispersed MB from suspension.

One recovery method is to fix the photocatalyst to a more readily recoverable material such as zeolite or carbon fiber [10,19], but the photocatalytic performance tends to be diminished due to reduced light irradiation and interactions with the carrier media [20,21]. Magnetic nanoparticles combined with photocatalysts can be easily separated

* Corresponding author at: Department of Environmental Science & Engineering, Fudan University, Shanghai 200438, PR China.
E-mail address: andong@fudan.edu.cn (D. An).

https://doi.org/10.1016/j.seppur.2023.124140
Received 27 March 2023; Received in revised form 9 May 2023; Accepted 18 May 2023
Available online 24 May 2023

Fig. 1. Process flow diagram for synthesizing photocatalyst.

from water without affecting their photocatalytic performance [22]. Nontoxic Fe_3O_4 occurs naturally and contains both Fe^{2+} and Fe^{3+} in its structure. The inverse spinel structure of $Fe^{3+}[Fe^{2+}Fe^{3+}]O_4^{2-}$ is beneficial for electron transfer as a narrow-bandgap semiconductor [23]. Fe_3O_4 nanoparticles also exhibit superparamagnetic behavior at standard temperature and pressure. Further, the addition of Fe oxides can significantly extend the photoresponse range of wide-band gap semiconductors [24]. For example, when exposed to visible light, addition of Fe_3O_4 to a photocatalyst resulted in faster pollutant degradation kinetics compared to the same photocatalyst without Fe_3O_4 [25]. There has not been, however, any focus on developing a magnetic composite Fe_3O_4/MoS_2/BiOI (FMB) photocatalyst for visible-light-driven (VLD) disinfection.

On the other hand, there is little research on the bactericidal mechanism of Bi-based photocatalyst. Existing technologies mainly focus on the degradation of bacteria before and after photocatalyst treatment [26]. Therefore, other technologies should be developed to accurately tell the exact story of the bacterial degradation during the process. To better understand the disinfection mechanism, molecular biology and instrumentation analysis technologies must be combined. Overall, the purpose of this study is to synthesize magnetic separable BiOI/MoS_2 microspheres that can disinfect microorganisms when exposed to visible light. The actual application potential was explored by applying it to the water source water of a drinking water treatment plant in Shanghai, China. Finally, the main disinfection mechanism was revealed by examining the effects of the photocatalyst on the cellular molecular and transcriptomic levels during the process.

2. Materials and methods

2.1. Synthesis and characterization of Fe_3O_4/MoS_2/BiOI microspheres

Details of the reagents used in this study are provided in Text S1. Bi$(NO_3)_3$ reacts with KI to form BiOI under hydrothermal conditions. Synthesis of MB with a mass ratio of MoS_2 to BiOI of 0.01 was carried out according to a previous study with slight modification [15]. According to the amount of MoS_2, the acquired photocatalysts were denoted as $M_{0.005}B$, $M_{0.01}B$ and $M_{0.02}B$. Subsequently, Fe_3O_4 modified MB microspheres were prepared by a hydrothermal method. Text S2 provides a detailed description of the fabrication process for BiOI, MB, and FMB, as illustrated in Fig. 1.

The morphology of the photocatalyst was determined by a scanning electron microscopy (SEM, Nova NanoSem 450, FEI). The crystalline structures and the valence states of the catalyst were characterized by powder X–ray diffraction (XRD, Bruker D2 PHASER) and X–ray photoelectron spectroscopy (XPS, Perkin Elmer PHI 5000C). The UV–visible diffuse reflectance spectrum (DRS) was measured using a UV–vis spectrophotometer (UV-2600, Shimadzu) with barium sulfate as the reference. The optical band gap energies (E_g) of samples were calculated by the Kubelka-Munk function [27]:

$$\alpha h\nu = A(h\nu - E_g)^{n/2} \quad (1)$$

where a, h, ν, E_g and A are the absorption coefficient, Planck constant, light frequency, band gap, and a constant, respectively. n is a constant which is dependent on the optical transition of a semiconductor (for direct transition, n = 1; for indirect transition, n = 4). The valence band value (E_{VB}) and conduction band value (E_{CB}) of photocatalyst are calculated by equations (2) and (3) [27]:

$$E_{VB} = X - E_e + 0.5E_g \quad (2)$$

$$E_{CB} = E_{VB} - E_g \quad (3)$$

X represents the absolute electronegativity of the semiconductor (for BiOI, MoS_2 and Fe_3O_4, the X values are respectively 6.20, 5.32 and 5.78 eV) and E_e represents the energy of free electrons on the hydrogen scale (4.5 eV).

2.2. Photocatalytic disinfection performance

A gram-negative strain of *E. coli* K-12 (ATCC 25922) was selected as the indicator bacteria to test the photocatalytic activity of the prepared FMB and to facilitate comparison to previously published literature. Details about the preparation of bacteria growth and stock suspensions can be found in Text S3. The prepared bacteria stock concentration was typically $1.0x10^8$ CFU/mL.

For VLD disinfection experiments, a UV cutoff filter ($\lambda \geq 400$ nm) was placed in the light path to exclude the UV portion of the light source (Xenon lamp, 500 W, XE-JY500, Beijing NBeT Co.). The distance between the light source and liquid level of the untreated water was 20 cm and the light intensity on the surface of the reaction suspension was 30 mW/cm^2 as measured by radiometer (TES1333, TES Electrical Electronic Corporation). In a 100 mL quartz beaker, 7.5 mg of photocatalyst was dispersed in 49.5 mL sterilized saline (15 mM NaCl, pH = 7) by 10 min of sonication. Following, 0.5 mL of bacteria stock suspension was added to reach an initial bacteria concentration of 10^6 CFU/mL. Prior to irradiation, the suspension was stirred for 10 min to achieve adsorption–desorption equilibrium. The temperature of the reaction system was maintained at 25.0 ± 0.1 °C by the circulating water between the double wall of the reaction beaker.

During irradiation, the solution was stirred continuously via stir bar

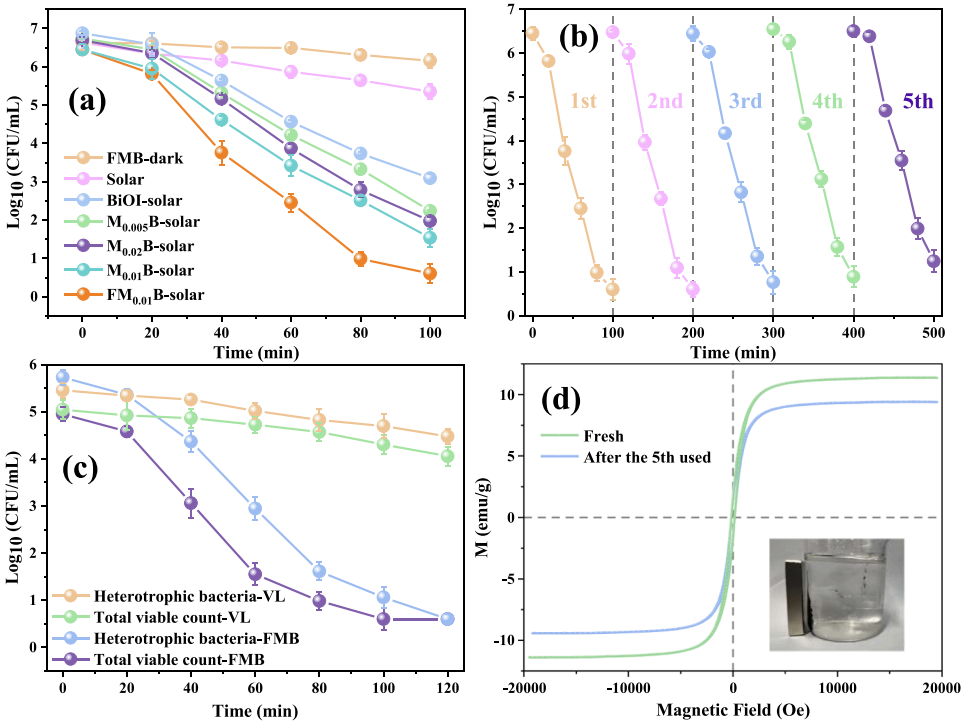

Fig. 2. (a) Disinfection of *E. coli* by 150 mg/L as-prepared photocatalyst irradiated with visible light or in the absence of light; (b) Recycling tests for FMB photocatalytic inactivation of *E. coli* by 150 mg/L FMB; (c) Raw water disinfection without FMB or with FMB (150 mg/L) under visible light irradiation; (d) magnetization curves of the fresh and used FMB.

with a stirring rod at 300 r/min. At given time intervals 0.1 mL of the reaction suspension was collected. Viable cell density was determined by the standard plate count method [28]. Serial 10–fold dilutions were performed and 0.3 mL of the diluted samples were evenly spread on a LB petri dish and cultured at 37 °C for 16 h. CFU on the plate was then counted. Based on the application of 0.3 mL and the need for at least one CFU to be present for detection, the detection limit (DL) was 4 CFU/mL. Blank control experiments were performed without photocatalyst, dark control experiments were conducted without irradiation. Each set of the experiments was conducted in triplicate. The average of results is shown in the figures and the standard deviation of triplicate experiments are shown as the error bars.

The potential for FMB recovery and reuse was investigated by cycling experiments. After evaluating the disinfection efficacy of FMB in an initial cycle, FMB was recovered by placing a magnet outside of the flask and decanting the remaining suspension. FMB was washed with 70% ethanol solution and deionized water three times to remove residual bacteria. FMB was then dried at 70 °C overnight and used again in the following experimental cycle. The crystalline structure and the magnetization curves of the virgin FMB and FMB which had been used five times were characterized by XRD, fourier transform infrared (FTIR), and a vibrating sample magnetometer (VSM, LakeShore 7404, USA).

Source water samples were collected from the intake of a conventional drinking water treatment plant in Shanghai treating Yangtze River water. The water samples were collected in amber glass bottles and stored at 4 °C. Raw water quality characteristics are listed in Text S4.

2.3. Photochemical reaction processes

To understand the potential for photocorrosion of FMB and loss of metal ions to the aqueous phase, which may act to directly inactivate the bacteria, 7.5 mg FMB was added into 50 mL sterilized deionized water and irradiated with visible light. Three 2 mL samples were collected after 100 min and filtered with 0.22 μm membranes. Concentrations of Bi^{3+}, Mo^{4+} and Fe^{3+} were determined by inductively coupled plasma optical emission spectroscopy (ICP-OES, Optima 8000, PerkinElmer, USA).

The disinfection mechanism of FMB was explored with scavenging experiments. Sodium oxalate (1 mM), 4-hydroxy-2,2,6,6-tetramethylpiperidine 1-oxyl free radical (TEMPOL, 0.2 mM), isopropanol (IPA, 0.05 mM), Fe(II)-ethylene diamine tetraacetic acid (EDTA) (0.05 mM), potassium chromate (0.2 mM) and histidine (1 mM) were used to scavenge h^+/•$OH_{surface}$, •O_2^-, •OH, H_2O_2, e^-, and $^1O_2$, respectively. Electron paramagnetic resonance (EPR) spectroscopy analysis was conducted with a JEOL-FA200 spectrometer and 5,5-dimethyl-1-pyrroline *N*-oxide (DMPO) and 4-amino-2,2,6,6-tetramethylpiperidine (TEMP) as spin traps [14,29]. The concentration of H_2O_2 was determined by titanium potassium oxalate method [28]. The level of statistical significance in paired sample *t*-test was set to 5%.

A semipermeable membrane system was used to separate the *E. coli* suspension and FMB to elucidate the roles of h^+ and e^- compared to diffuse reactive oxygen species (ROS). The molecular weight cutoff of the semipermeable membrane was 8000–12000 Da, which inhibited passing of *E. coli* cells and FMB, but did not affect the movement of water and ROS.

2.4. Analytical methods for understanding inactivation

SEM was used to visualize changes in bacteria morphology. Detailed descriptions of the method are provided in Text S6. For the measurement of K^+ leakage from *E. coli* cells, at given intervals, 1 mL of the irradiated bacteria suspension was centrifuged and the supernatant was analyzed by inductively coupled plasma mass spectrometry (ICP-MS, NexION 300D, PerkinElmer, USA). The activity of β-GAL was calculated by measuring absorption of 400 nm light via spectrometer (i.e., β-GAL endoenzyme in bacteria decomposed by p-nitrobenzene-β-D-galactopyranose to p-nitrophenol, which has a maximum absorption peak at 400 nm). Superoxide dismutase (SOD) activity was measured using SOD WST-8 Assay Kits (S0101, Beyotime, China), and the catalase (CAT)

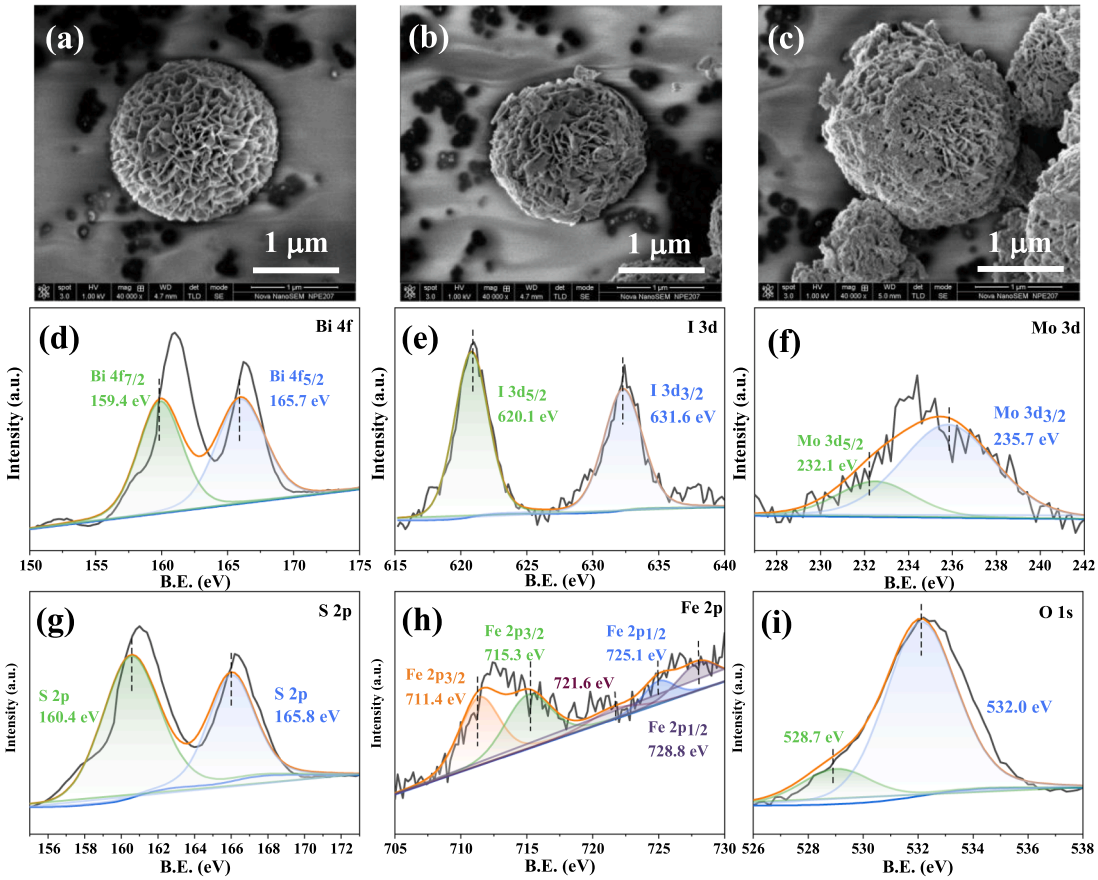

Fig. 3. (a-c) SEM images of BiOI, MB and FMB, respectively; (d-i) The XPS spectra of Bi 4f, I 3d, Mo 3d, S 2p, Fe 2p and O 1 s for FMB, respectively.

activity was evaluated with Catalase Assay Kits (S0051, Beyotime, China). The determination of the zeta potential and particle size of bacteria was carried out using the Zetasizer Nano ZS (Malvern Instrument) both before and after treatment.

The determination of the cell surface hydrophobicity of *E. coli* was carried out using the microbial adhesion to hydrocarbons method. To do this, 1 mL of bacterial suspensions were sampled at specific time intervals and mixed with 0.4 mL of n-hexane. After 15 min of standing, the mixture was separated into two phases, and the absorbance at 600 nm of the lower phase was measured. A phosphate buffer solution (PBS) was used as a blank control. The cell surface hydrophobicity value was determined using equation. (4).

$$\text{Cell surface hydrophobicity} = \frac{Control_{600nm} - Test_{600nm}}{Control_{600nm}} \quad (4)$$

2.5. Transcriptomics

E. coli and 150 mg/L FMB were dispersed in 100 mL saline solution (15 mM NaCl, pH = 7). After irradiation for 40 min, the bacteria suspensions were separated by centrifugation at 8000 r/min for 5 min. *E. coli* was also irradiated alone as a control. The extraction of the total RNA, fragmentation of mRNA, and sequencing with an Illumina HiSeq xten platform were performed by Shanghai Majorbio Bio-pharm Technology Co., Ltd (Shanghai, China). High-quality RNA samples (OD260/280 = 1.8–2.2, RIN > 6.5, RNA concentration > 100 ng/μL) were used to construct a sequencing library. To identify significantly differentially expressed genes (DEGs) between samples, the expression level of each transcript was calculated according to the transcripts per million reads method [1]. Gene function was annotated and enriched by gene ontology (GO) terms and Kyoto Encyclopedia of Genes and Genomes (KEGG) [1].

3. Results and discussion

3.1. Disinfection performance of as-prepared photocatalysts

Performance of the photocatalysts was first assessed at a fixed concentration of 150 mg/L catalyst by measuring the reduction of *E. coli* viability after exposure of a catalyst/*E. coli* mixed solution to visible light. In control experiments with the photocatalyst but without light, the cell density of *E. coli* was slightly decreased at longer durations (e.g., 160 min) when exposed to BiOI, MB, or FMB, potentially due to *E. coli* adsorption to the photocatalyst surface (Fig. 2a and Text S7). In the control experiment without using photocatalysts but under illumination, the survival rate of *E. coli* only decreased by 19% after exposure for 100 min. However, when *E. coli* was irradiated with photocatalyst for 100 min, the removal of *E. coli* by $M_{0.01}B$ was 1.56 CFU/mL, 0.706 CFU/mL, and 0.4413 CFU/mL higher than that by BiOI, $M_{0.005}B$, and $M_{0.02}B$, respectively, indicating that the photocatalytic performance of $M_{0.01}B$ was the best among these materials. This may be due to the improved separation of photogenerated charge carriers in BiOI photocatalyst by loading MoS_2, while excessive loading of MoS_2 will block the active sites of photocatalytic reaction and lead to the decrease of photocatalytic performance [15]. Moreover, further modification of $M_{0.01}B$ with Fe_3O_4 can completely inactivate *E. coli* in the system within 100 min. We have also reviewed a number of photocatalytic disinfection research studies and compared their disinfection properties (Text S9). Compared to most reported photocatalysts, FMB exhibits a superior disinfection effect.

In Fig. 2b we show that there was no or little change in the photocatalytic inactivation of *E. coli* over 5 cycles of irradiation followed by magnetic FMB recovery and cleaning. The slight decrease in the sterilization efficiency observed during the 5th cycle (90 % reduction in CFU/mL compared to 100 % in the first run) may be due to the incomplete

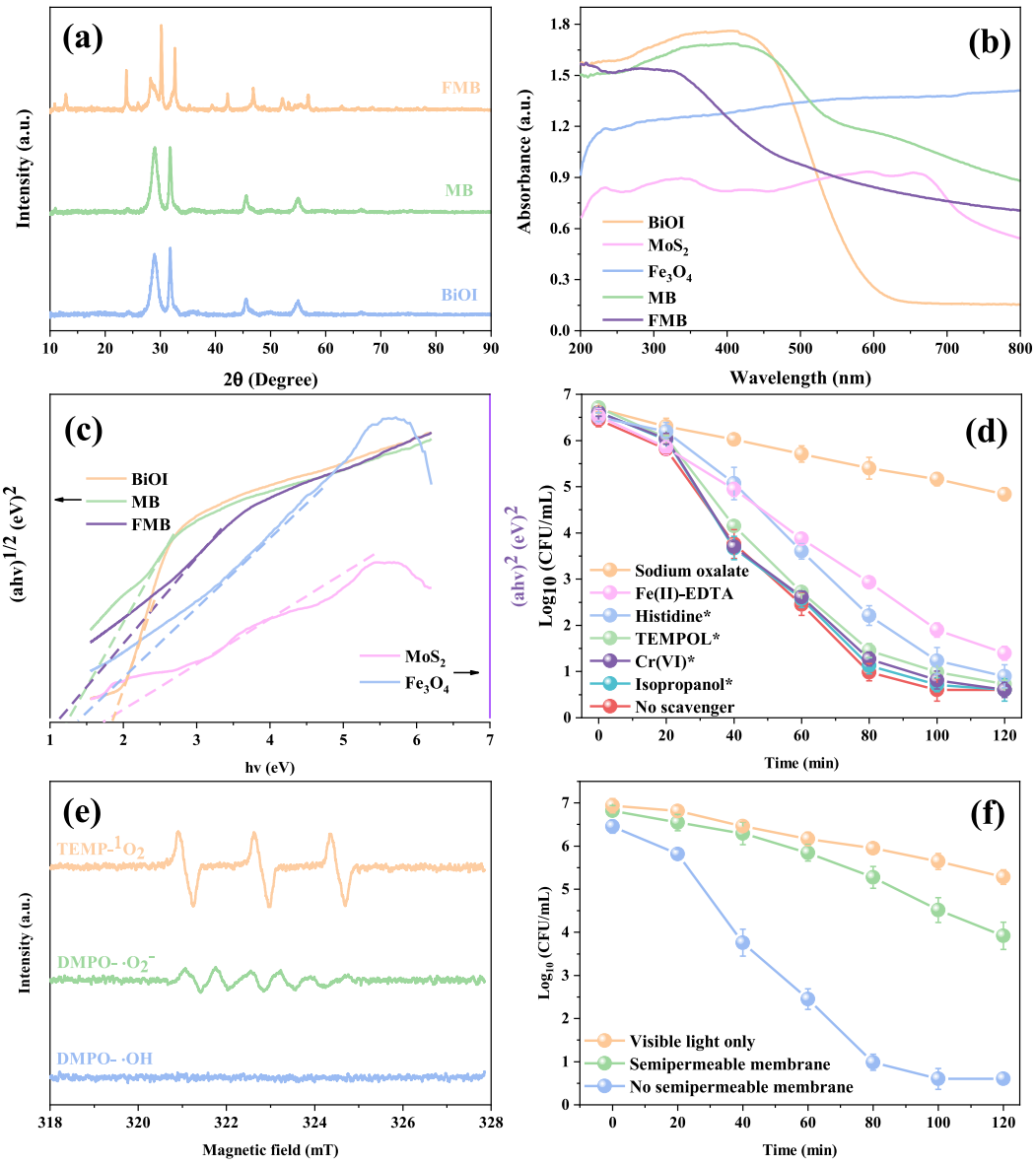

Fig. 4. (a) XRD diffractogram, (b) DRS spectra, and (c) Bandgaps of the obtained photocatalyst; (d) Disinfection efficiency by FMB in the presence of different scavengers under irradiation, paired t-tests were performed at the 95% confidence level. * indicates $p < 0.05$ for a paired *t*-test between the indicated experiment and the control without a scavenger; (e) EPR spectra of TEMP-$^1O_2$, DMPO-•O_2^- and DMPO-•OH after irradiation for 60 min in the presence of FMB; (f) Disinfection by FMB in a membrane system which separated irradiated FMB and the *E. coli*.

removal of bacterial fragments absorbed to the surface of FMB, blocking surface active sites. The FTIR and XRD peak positions of FMB were not significantly shifted before and after being used for the fifth time, as displayed in Text S10. Based on this result, we believe that the photodegradation of FMB is not significant during the photocatalytic process, and the crystal structure remains intact without changes.

To understand the potential for practical application in drinking water treatment, disinfection of total viable cell count and heterotrophs were assessed in a sample of water taken from a reservoir which acts as the source water for a drinking water treatment plant in Shanghai. In Fig. 2c we show that the total viable count and heterotrophic bacteria in raw water were completely inactivated after photocatalytic treatment of 100 and 120 min, respectively. Fig. 2d shows that the magnetic properties of the sample did not fade too much after 5 times of application, and could still be easily recovered by applied magnetic field (inset). Overall, the potential for reuse and longevity of the material were demonstrated. Experiments of water disinfection with raw water show that FMB was easy to recover and had good disinfection efficacy even after repeated use. Although the irradiation time needed for disinfection is somewhat long and thus likely precludes its use at centralized drinking water treatment facilities, FMB would be highly useful for off-grid treatment scenarios such as disaster relief, where repeated shipment and storage of oxidant disinfecting chemicals is not practical.

3.2. Characterization of photocatalyst and photochemical reaction processes

The morphology and structure of the synthesized photocatalysts were investigated by SEM. As shown in Fig. 3a, the 3D flower-like BiOI microspheres were ~ 1.7 μm in diameter and were tightly assembled by intersecting nanosheets. The surface of pure BiOI was evenly covered with abundant nanopores. When MoS_2 was deposited on the surface of BiOI (Fig. 3b), no fragments of MoS_2 were found around the MB microspheres, indicating that MoS_2 crystalline nucleus was formed and grew in-situ on the surface of BiOI. When Fe_3O_4 was deposited onto the surface of MB, the diameter increased slightly and there was a visible

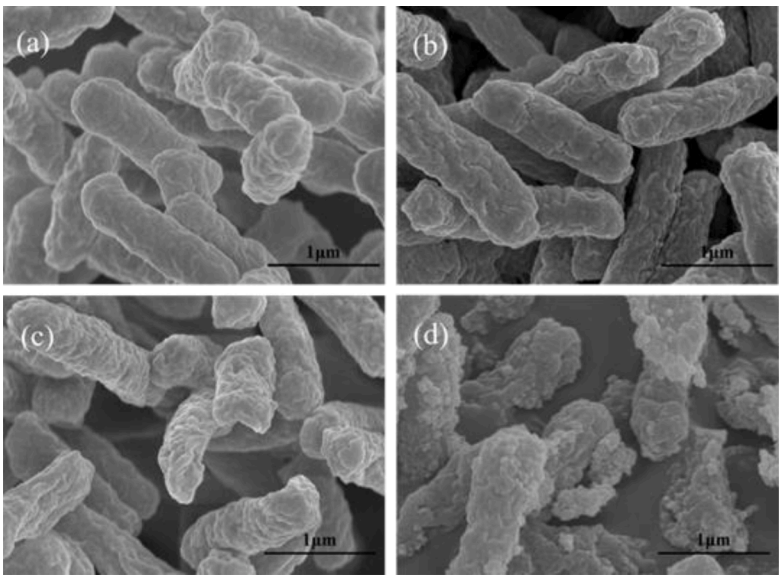

Fig. 5. SEM images of *E. coli* cells after 0 min (a), 20 min (b), 40 min (c), and 100 min (d) of irradiation in the presence of FMB.

increase in the number of nanosheets (Fig. 3c). By energy dispersive X-ray spectroscopy (EDS) (Text S11), Bi, Mo and Fe were homogeneously distributed throughout the flower-like structure.

The surface electronic state and chemical composition of FMB were also surveyed by XPS. From the Bi 4f spectra (Fig. 3d) two strong absorption peaks at 159.4 and 165.7 eV can be seen, which are indexed to Bi 4f 7/2 and Bi 4f 5/2, respectively. This suggests that the chemical valence state of Bi element in the FMB microspheres is + 3. For the I 3d (Fig. 3e), two typical peaks of I 3d 5/2 and I 3d 3/2 are located at 620.1 and 631.6 eV, respectively. This is the characteristic peak of I^- in the FMB samples. Mo 3d has two characteristic peaks at 232.1 and 235.7 eV, corresponding to Mo 3d 5/2 and Mo 3d 3/2, respectively, indicating the feature of Mo^{4+} in FMB composites. In Fig. 3g, the peaks at 160.4 and 165.8 eV are attributed to the 2p state of S in MoS_2. Similarly, two characteristic peaks located at 711.4 and 715.3 eV belong to Fe 2p 3/2, while two peaks observed at 725.1 and 728.8 eV belong to Fe 2p 1/2, and correspond to Fe (II) and Fe (III) in Fe_3O_4. The peak at 721.6 eV belongs to the satellite peak of Fe (III). The O 1 s spectrum of FMB (Fig. 3i) shows two peaks at 531.0 and 528.7 eV attributable to adsorbed oxygen on the surface and the lattice oxygen, respectively. The above results further demonstrate that Fe_3O_4 and MoS_2 has been closely coupled with BiOI.

The phase and crystalline structure of the photocatalyst was characterized by XRD and the results are shown in Fig. 4a. Two diffraction peaks and two other weak peaks of BiOI were present at approximately 2θ of 29.6°, 31.7°, 45.4° and 55.2°, which correspond to the (102), (110), (200) and (212) planes, respectively. The results are in good agreement with the standard tetragonal phase BiOI phase diagram (JCPDS 00-010-0445). The diffraction peaks of MoS_2/BiOI at 2θ of 29.2°, 33.0°, 38.2°, 48.0°, 58.3° and 66.5° are representative of a typical hexagonal MoS_2 crystal with (003), (101), (104), (107), (110) and (116) planes (JCPDS 03-065-6963). The (110) plane of BiOI had a slight right shift (0.211°) due to in situ ion exchange between MoS_2 and BiOI. The diffraction peaks of the synthesized FMB were representative of BiOI, MoS_2 and Fe_3O_4, as expected. The diffraction peaks at 2θ of 14.9°, 23.7°, 30.1°, 32.0°, 43.1°, 47.2°, 53.4° and 56.1° correspond to a face-centered cubic structure with (010), (112), (114), (022), (220), (216), (314) and (231) planes (JCPDS 01-076-0956).

By DRS (Fig. 4b-c), the estimated bandgap energy of BiOI, MoS_2, Fe_3O_4, MB, and FMB were 1.84, 1.76, 1.37, 1.27, and 1.10 eV, respectively, suggesting that the incorporation of MoS_2 and Fe_3O_4 improved the transfer efficiency of BiOI photogenerated electrons. The calculated E_{VB} and E_{CB} of BiOI, MoS_2 and Fe_3O_4 are listed in Text S12, and demonstrate that they can form an effective overlapping band structure. Overall, we found that deposition of MoS_2 and Fe_3O_4 onto BiOI improved the visible light absorption and reduced the bandgap of the photocatalyst.

In photocatalytic reactions, the release of cytotoxic metal ions from semiconductor photocatalysts can cause bacterial inactivation [5]. The inherent toxicity of metal ions released during the FMB treatment process was studied. After irradiation for 100 min, the concentrations of Bi^{3+}, Mo^{4+} and Fe^{3+} in the solution were 2.17 μg/L, 0.91 μg/L, and 0.02 mg/L, respectively. When the same concentration of metal ions was added to solution and kept for the same time, the number of viable bacteria did not change compared to the sample without metal ions (Text S13). Therefore, the leakage of metal ions in photocatalytic reactions is not the main mechanism of *E. coli* inactivation in this study.

Strongly oxidizing active species such as e^-, h^+, •OH, H_2O_2, $\bullet O_2^-$ and $^1O_2$ have been reported to be produced during photocatalysis and decompose the cell membranes, leading to microbial inactivation [14]. To further understand which reactive species drive inactivation, experiments were conducted with scavengers. The toxicity of scavengers on *E. coli* cells was initially investigated; none of the scavengers affected the viability of *E. coli* (Text S14). Addition of oxalate (h^+ scavenger) and chromate (e^- scavenger) substantially reduced the inactivation of *E. coli*, suggesting that h^+ and e^- played a prominent role (Fig. 4d). Fe(II)-EDTA (H_2O_2 scavenger), also significantly decreased inactivation although less than oxalate and chromate. Addition of TEMPOL ($\bullet O_2^-$ scavenger) and histidine ($^1O_2$ scavenger) resulted in slight inhibition of the bacteria inactivation process, and together these results suggest that H_2O_2, $\bullet O_2^-$ and $^1O_2$ play a limited role in the inactivation. The addition of isopropanol (•OH scavenger) did not significantly suppressed inactivation. •OH therefore does not play a role in inactivation, which agrees with the results from EPR (Fig. 4e and Text S15), where no •OH was present. On account of Eq. (12), most of the low concentration of •OH is further converted into $^1O_2$, undetected. These findings confirmed the formation of $^1O_2$ and $\bullet O_2^-$ in the irradiated FMB suspension, which provides reliable evidence that photo-generated holes and electrons are effectively separated and reacted with adsorbed oxygen to produce a series of active species, and ultimately induced photocatalytic disinfection by Eq. (5) (13) [14]. Thus, the species responsible for *E. coli* inactivation were h^+ and e^-. H_2O_2, $^1O_2$ and $\bullet O_2^-$ are also present and cause inactivation, but to a lesser extent.

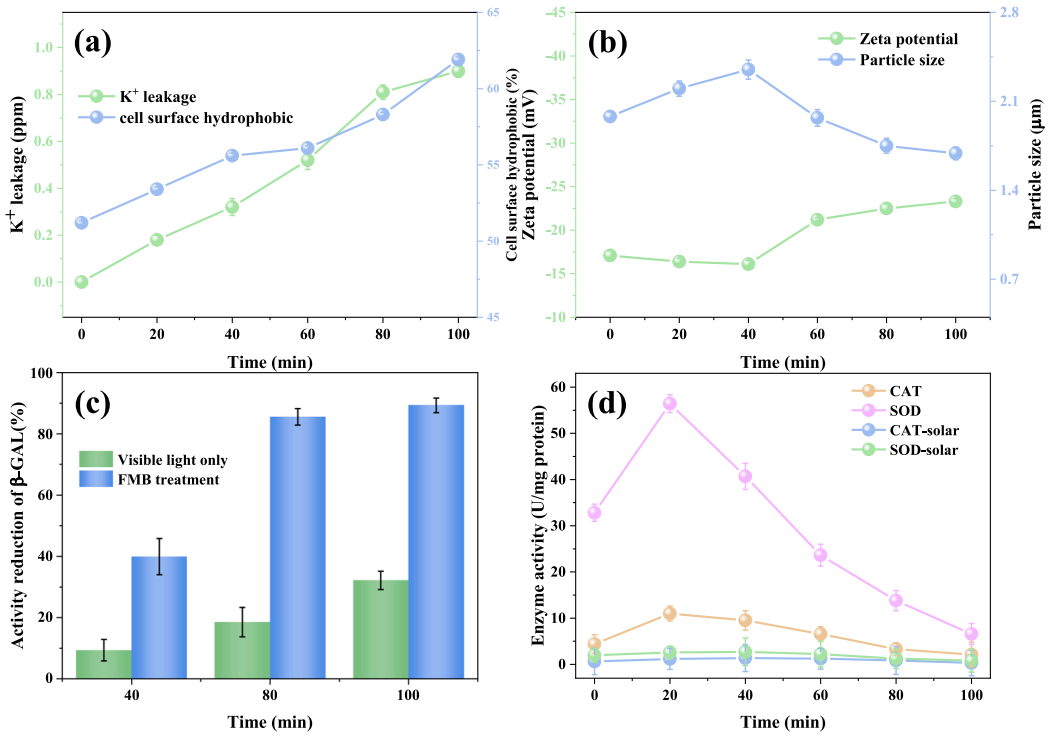

Fig. 6. (a) K^+ leakage concentration and cell surface hydrophobicity of *E. coli* after irradiation with FMB; (b) Changes of zeta potential and particle size of *E. coli* after irradiation with FMB; (c) Changes of β-GAL activity over time with FMB irradiation; (d) Changes of *E. coli* COD and SOD activity during irradiation with FMB.

$$FMB + visiblelight \rightarrow FMB^* + h^+ + e^- \quad (5)$$

$$O_2 + e^- \rightarrow \bullet O_2^- \quad (6)$$

$$\cdot O_2^- + h^+ \rightarrow {}^1O_2 \quad (7)$$

$$\bullet O_2^- + H^+ \rightarrow \bullet OOH \quad (8)$$

$$\bullet OOH + H^+ + e^- \rightarrow H_2O_2 \quad (9)$$

$$2\cdot O_2^- + 2H^+ \rightarrow H_2O_2 + {}^1O_2 \quad (10)$$

$$\cdot O_2^- + H_2O_2 \rightarrow {}^1O_2 + OH^- + \cdot OH \quad (11)$$

$$\cdot O_2^- + \cdot OH \rightarrow {}^1O_2 + OH^- \quad (12)$$

$$h^+ + e^- + H_2O_2 + {}^1O_2 + \cdot O_2^- + E.\ coli_{live} \rightarrow E.\ coli_{dead} \quad (13)$$

In a final experiment to confirm the importance of direct reactions between h^+, e^-, and the cells, FMB was suspended separated from the bacteria suspension by a semipermeable membrane that neither the FMB microspheres (2.0–2.5 μm in size) or the bacteria cells (2.0 × 0.5 μm) were able to pass. Thus, the system allows only water molecules and diffusing active species to pass the membrane [14], inhibiting reactions between h^+/e^- on the FMB surface and *E. coli*, but allowing reactions with diffuse ROS. In Fig. 4f, we show that the cell density was slightly reduced after 120 min of irradiation, and this further demonstrates that surface h^+ and e^- play crucial roles while H_2O_2, $^1O_2$ and $\bullet O_2^-$ contribute, but to a much lesser extent.

3.3. Molecular mechanisms of bacterial integrity disruption

To further study the molecular mechanism of FMB photocatalytic bacteria inactivation, the integrity of the cell membrane and the release of intracellular substances was explored. Prior to irradiation, the *E. coli* cells were rod-like shaped with an intact and smooth bacterial membrane (Fig. 5a). After 20 and 40 min of photocatalytic treatment with FMB, the surface of *E. coli* began to deform and was visibly damaged (Fig. 5b-c). At longer irradiation time points the cells were visibly damaged to greater extents and no longer rod-shaped (Fig. 5d).

In Fig. 6a we show an increase in K^+ leakage from *E. coli* when irradiated with FMB system. In addition, the development of photocatalytic processes has led to a notable rise in the hydrophobicity of *E. coli*. This is attributed to the adherence of internal organic materials onto the surface of the cells, which are released when the cell wall and membrane fail. Overall, the above experiments indicate that the loss of membrane integrity and the resultant leakage of intracellular substances.

Zeta potential is a way to measure the electrical potential of the interface between fluid and bacteria cells. During treatment, the bacteria's surface charge can change due to ionization and adsorption of ions from the solution. The cell wall and membranes also affect the overall charge. Further understanding of the changes in bacteria during disinfection can be obtained through analysis of Zeta potential and cell size measurement. The initial Zeta potential of E. coli before treatment was −17.1 mV, and their size was 1.98 μm. As shown in Fig. 6b, during the photocatalytic process, the Zeta potential initially decreased before increasing again, while the average particle size increased before decreasing. Changes in membrane potential can affect the stability and integrity of the cell membrane. The release of intracellular components during disinfection and the presence of sodium chloride in water cause functional groups on the cell surface membrane to bind with cations in water, resulting in an "electrically neutralized" phenomenon [30,31]. Bacterial colloids may aggregate due to instability. However, as the outer membrane phospholipid bilayer is destroyed and phosphate is ionized, the absolute value of the Zeta potential of the cell increases, the repulsion between bacteria increases, cell aggregation decreases, and the interaction between active species and cells is promoted. For the average particle size, the decrease in the absolute value of the Zeta potential on the cell surface leads to cell aggregation and an increase in particle size. However, as disinfection proceeds, E. coli is oxidized by strong oxidative active species, resulting in cell fragments and a

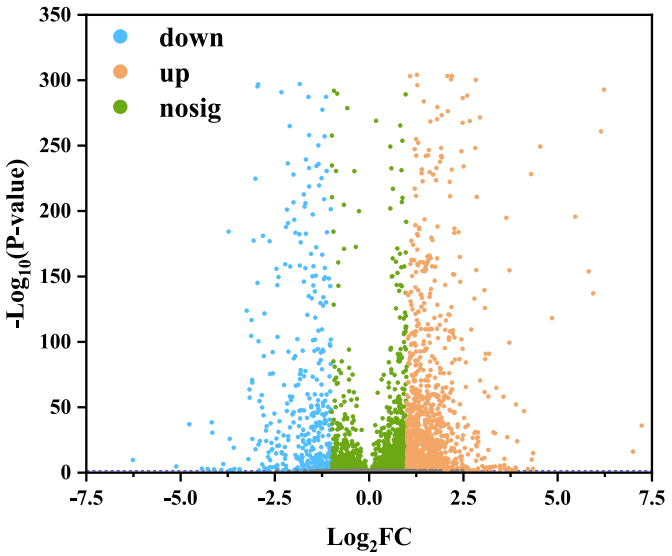

Fig. 7. Differentially expressed genes of *E. coli* after FMB irradiation shown as a volcano plot of transcriptomic analysis.

decrease in the average particle size.

Damage to the inner membrane was evaluated by measuring the change of β-GAL activity. In Fig. 6c we show that both irradiation alone and photocatalytic treatment contributed to β-GAL inactivation. The presence of FMB caused a 57% greater loss of β-GAL activity over the control with visible light irradiation after 100 min. This is likely due to reactive species passing both the outer and inner membranes and reacting with enzyme. To further confirm disruption of the inner membrane, SOD and CAT enzymatic activity was measured. SOD catalyzes the dismutation of $\bullet O_2^-$ to H_2O_2 or O_2, while CAT catalyzes the decomposition of H_2O_2 into H_2O and O_2 [32]. With FMB present, CAT activity increased in the first 20 min of irradiation but then decreased, likely due to complete loss of cell viability (Fig. 6d).

3.4. Transcriptomic analysis

To gain further insight into the underlying bacteria inactivation mechanism of FMB, gene expression after 40 min of photocatalytic treatment were assessed. The results were compared to those of visible light irradiation without photocatalyst (Transcriptome quality assessment is shown in Text S17). After filtering and normalization, 5089 genes were analyzed. Overall, 1779 genes were differentially expressed in *E. coli* exposed to visible light in the presence of FMB ($|\log2\ FC| \geq 1$; $p_{adjust} < 0.05$). Of these, 495 genes were downregulated and 1284 genes were upregulated (Fig. 7). The top 5 gene functions with the greatest degree of enrichment by Gene Ontology (GO) analysis were nucleoside monophosphate metabolism, organophosphate biosynthesis, ribose phosphate biosynthesis, translation, and purine-containing compound biosynthesis (Fig. 8).

We suspected that FMB photocatalysis likely caused oxidative stress. Several genes involved in the defense against oxidative stress were upregulated and are part of the OxyR regulon (e.g., *ahpC*, *dps*, *gor*, *katG*, *sufA*, *sufB*, *sufC*, *sufD* and *sufS* (Text S18). The following were also upregulated: *trxC*, encoding the oxidative-defense related thioredoxin 2; *soxR*, regulating transcription of genes involved in antioxidant stress and other cellular processes, such as membrane permeability; *zntA*, encoding a metal efflux pump that can remove heavy metals and reduce the toxicity of heavy metals to cells; *marR*, a transcriptional regulator of genes involved in the defense against oxidative stress and several other stresses. Downregulation of *sucA* expression was also observed and indicates the accumulation of 2-oxoglutarate, which is connected to oxidative stress protection [33–36]. These results further demonstrate that the cellular membrane integrity is compromised by reactive species produced by irradiation of FMB and that subsequent oxidative stress occurs.

3.5. Disinfection mechanism

Based on the results of inactivation performance, subcellular damage, and transcriptomics, the mechanism of FMB photocatalytic bacterial inactivation can be proposed as follows: i) FMB generates electron-hole pairs under irradiation and further produces highly oxidative active species such as H_2O_2, $^1O_2$, and $\bullet O_2^-$, and direct contact between the

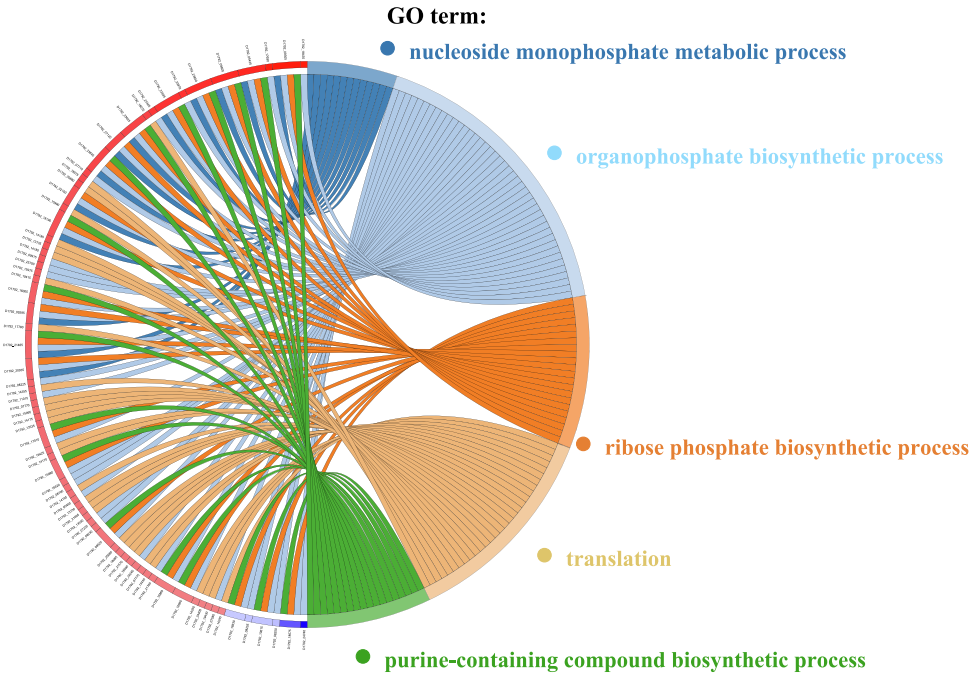

Fig. 8. String diagram of the top five functions of GO enrichment after FMB irradiation.

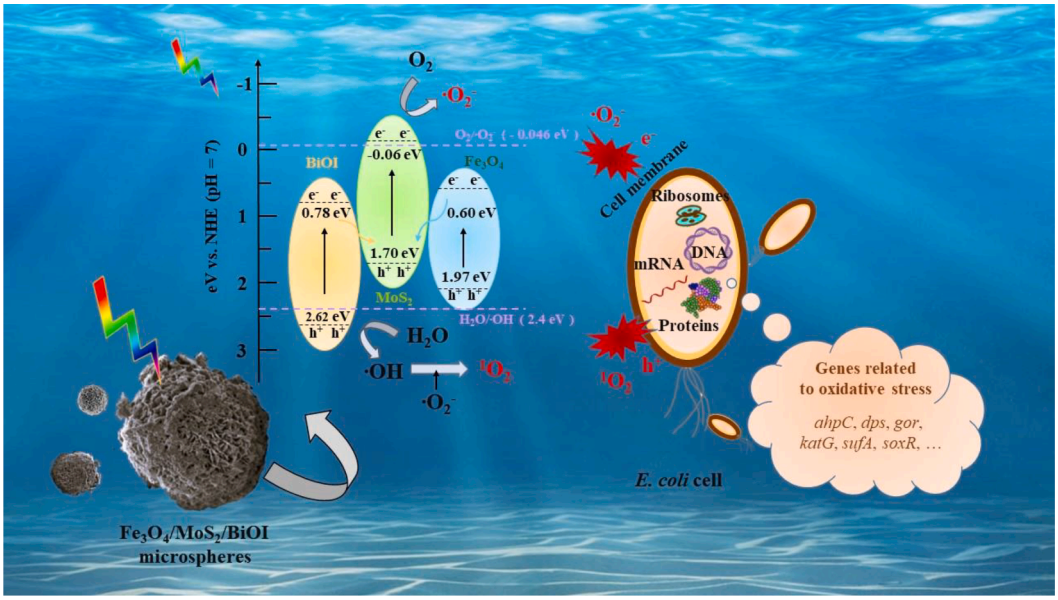

Fig. 9. The schematic presentation of the electronic transfer mechanism of FMB for water disinfection.

photocatalyst and bacteria is crucial for the maximum disinfection performance of the system; ii) Highly oxidative active species primarily destroy the cell membrane and surface components of bacteria, leading to damage to cell integrity, leakage of intracellular contents, and a decrease in key enzyme activity; iii) Transcriptomic analysis revealed that light-induced active species affected the expression of oxidative stress-related genes in *E. coli*, leading to its inactivation. The schematic diagram of electron transfer and inactivation mechanism of the photocatalyst during the photocatalytic process is shown in Fig. 9.

4. Conclusions

A novel magnetically recoverable FMB photocatalyst was successfully prepared for water disinfection. Complete disinfection of 1.0×10^6 CFU/mL *E. coli* was achieved under visible light illumination for 100 min. The excellent disinfection efficiency of the FMB in a raw water source established the potential for application to drinking water disinfection, particularly in scenarios where other disinfectants are not practical (e.g., disaster relief, off-grid point of use,) and longer required treatment time is acceptable. The inactivation mechanism was ascribed to photogenerated active species rather than leakage of cytotoxic metal ions. Throughout the disinfection procedure, the zeta potential of the cells exhibited an initial decrease followed by an increase, and the particle size displayed an initial increase followed by a decrease, which implies that the cells underwent rupture. The disintegration of the *E. coli* cell membrane was verified through multiple means, including SEM, potassium ion leakage, and variations in cell surface hydrophobicity and hydrophilicity at the molecular level. β-GAL activity decreased and the abundance of antioxidant enzymes increased, suggesting the antioxidant cellular system was damaged. Transcriptomics further revealed that *E. coli* cells are subject to oxidative stress. We believe these findings will help to understand the mechanism of solar photocatalytic disinfection and the practical development of this technology.

CRediT authorship contribution statement

Yijun Shi: Conceptualization, Methodology, Investigation, Writing – original draft, Visualization. **Jiaxin Ma:** Writing – review & editing. **David Hanigan:** . **Yanan Chen:** . **Yunkun Qian:** Validation, Data curation, Investigation. **Jun Guo:** Validation, Data curation, Formal analysis. **Dong An:** Conceptualization, Resources, Supervision, Project administration, Funding acquisition.

Declaration of Competing Interest

The authors declare that they have no known competing financial interests or personal relationships that could have appeared to influence the work reported in this paper.

Data availability

Data will be made available on request.

Acknowledgements

This research is supported by the National Natural Science Foundation of China (NSFC 22076026, 21777031, 21577024) and partially supported by the National Science Foundation under Grant No. 1804255.

Appendix A. Supplementary material

Supplementary data to this article can be found online at https://doi.org/10.1016/j.seppur.2023.124140.

References

[1] L. Cai, X. Wei, H. Feng, G. Fan, C. Gao, H. Chen, X. Sun, Antimicrobial mechanisms of g-C_3N_4 nanosheets against the oomycetes Phytophthora capsici: disrupting metabolism and membrane structures and inhibiting vegetative and reproductive growth, J. Hazard. Mater. 417 (2021) 126121.
[2] Y. Jin, Y. Shi, Z. Chen, R. Chen, X. Chen, X.i. Zheng, Y. Liu, Combination of sunlight with hydrogen peroxide generated at a modified reticulated vitreous carbon for drinking water disinfection, J. Clean. Prod. 252 (2020) 119794.
[3] S. Das, A.J. Misra, A.P. Habeeb Rahman, B. Das, R. Jayabalan, A.J. Tamhankar, A. Mishra, C.S. Lundborg, S.K. Tripathy, Ag@SnO_2@ZnO core-shell nanocomposites assisted solar-photocatalysis downregulates multidrug resistance in Bacillus sp.: a catalytic approach to impede antibiotic resistance, Appl. Catal. B-Environ. 259 (2019) 118065.
[4] G. Subramanian, H. Prakash, Photo augmented copper-based fenton disinfection under visible LED light and natural sunlight irradiation, Water Res. 190 (2021) 116719.
[5] Y. Shi, J. Ma, Y. Chen, Y. Qian, B. Xu, W. Chu, D. An, Recent progress of silver-containing photocatalysts for water disinfection under visible light irradiation: a review, Sci. Total Environ. 804 (2022) 150024.

[6] W. Zhu, J. Liu, S. Yu, Y. Zhou, X. Yan, Ag loaded WO_3 nanoplates for efficient photocatalytic degradation of sulfanilamide and their bactericidal effect under visible light irradiation, J. Hazard. Mater. 318 (2016) 407–416.
[7] S. Sontakke, C. Mohan, J. Modak, G. Madras, Visible light photocatalytic inactivation of Escherichia coli with combustion synthesized TiO_2, Chem. Eng. J. 189–190 (2012) 101–107.
[8] F. He, Z. Wang, Y. Li, S. Peng, B. Liu, The nonmetal modulation of composition and morphology of g-C_3N_4-based photocatalysts, Appl. Catal. B-Environ. 269 (2020) 118828.
[9] M. Fouad, M. Gar Alalm, H.K. El-Etriby, D.C. Boffito, S. Ookawara, T. Ohno, M. Fujii, Visible-light-driven photocatalytic disinfection of raw surface waters (300–5000 CFU/mL) using reusable coated Ru/WO_3/ZrO_2, J. Hazard. Mater. 402 (2021) 123514.
[10] Y. Zhang, A. Sun, M. Xiong, D.K. Macharia, J. Liu, Z. Chen, M. Li, L. Zhang, TiO_2/BiOI p-n junction-decorated carbon fibers as weavable photocatalyst with UV–vis photoresponsive for efficiently degrading various pollutants, Chem. Eng. J. 415 (2021) 129019.
[11] J. Yang, H. Su, Y. Wu, D. Li, D. Zhang, H. Sun, S. Yin, Facile synthesis of kermesinus BiOI with oxygen vacancy for efficient hydrogen generation, Chem. Eng. J. 420 (2021) 127607.
[12] A. Kumar, P. Singh, A.A.P. Khan, Q.V. Le, V.-H. Nguyen, S. Thakur, P. Raizada, CO_2 photoreduction into solar fuels via vacancy engineered bismuth-based photocatalysts: selectivity and mechanistic insights, Chem. Eng. J. 439 (2022) 135563.
[13] J. Liang, F. Liu, M. Li, W. Liu, M. Tong, Facile synthesis of magnetic Fe_3O_4@BiOI@AgI for water decontamination with visible light irradiation: different mechanisms for different organic pollutants degradation and bacterial disinfection, Water Res. 137 (2018) 120–129.
[14] J. Liang, C. Shan, X. Zhang, M. Tong, Bactericidal mechanism of BiOI–AgI under visible light irradiation, Chem. Eng. J. 279 (2015) 277–285.
[15] S. Guo, H. Luo, Y. Li, J. Chen, B. Mou, X. Shi, G. Sun, Structure-controlled three-dimensional BiOI/MoS_2 microspheres for boosting visible-light photocatalytic degradation of tetracycline, J. Alloy. Compd. 852 (2021) 157026.
[16] Y.u. Guan, J. Wu, Q. Liu, M. Gu, Y. Lin, Y. Qi, T. Jia, W. Pan, P. He, Q. Li, Fabrication of BiOI/MoS_2 heterojunction photocatalyst with different treatment methods for enhancing photocatalytic performance under visible-light, Mater. Res. Bull. 120 (2019) 110579.
[17] M.d. Ahmaruzzaman, V. Gadore, MoS_2 based nanocomposites: an excellent material for energy and environmental applications, J. Environ. Chem. Eng. 9 (5) (2021) 105836.
[18] L. Hao, P. Ju, Y.u. Zhang, X. Zhai, C. Sun, J. Duan, Y. Su, Z. Lu, D. Liao, Fabrication of hierarchical flower-like BiOI/MoS_2 heterostructures with highly enhanced visible-light photocatalytic activities, Colloid. Surface. A. 610 (2021) 125714.
[19] G. Hu, J. Yang, X.u. Duan, R. Farnood, C. Yang, J. Yang, W. Liu, Q. Liu, Recent developments and challenges in zeolite-based composite photocatalysts for environmental applications, Chem. Eng. J. 417 (2021) 129209.
[20] A. Beyhaqi, Q. Zeng, S. Chang, M. Wang, S.M. Taghi Azimi, C. Hu, Construction of g-C_3N_4/WO_3/MoS_2 ternary nanocomposite with enhanced charge separation and collection for efficient wastewater treatment under visible light, Chemosphere 247 (2020) 125784.
[21] D. Majhi, K. Das, A. Mishra, R. Dhiman, B.G. Mishra, One pot synthesis of CdS/BiOBr/$Bi_2O_2CO_3$: a novel ternary double Z-scheme heterostructure photocatalyst for efficient degradation of atrazine, Appl. Catal. B-Environ. 260 (2020) 118222.
[22] P. He, X. Zhao, F. Luo, Y. Zhang, J. Wei, T. Xu, J. Wu, N. Chen, Magnetically recyclable Fe_3O_4 doped flower-like MoS_2: efficient removal of elemental mercury, Fuel 282 (2020) 118728.
[23] S. Li, Q. Ma, L. Chen, Z. Yang, M. Aqeel Kamran, B. Chen, Hydrochar-mediated photocatalyst Fe_3O_4/BiOBr@HC for highly efficient carbamazepine degradation under visible LED light irradiation, Chem. Eng. J. 433 (2022) 134492.
[24] A.G. Leonel, A.A.P. Mansur, H.S. Mansur, Advanced functional nanostructures based on magnetic iron oxide nanomaterials for water remediation: a review, Water Res. 190 (2021) 116693.
[25] R. Wang, R. Liu, S. Luo, J. Wu, D. Zhang, T. Yue, J. Sun, C. Zhang, L. Zhu, J. Wang, Band structure engineering enables to UV-Visible-NIR photocatalytic disinfection: mechanism, pathways and DFT calculation, Chem. Eng. J. 421 (2021) 129596.
[26] R. Kumar, P. Raizada, N. Verma, A. Hosseini-Bandegharaei, V.K. Thakur, Q.V. Le, V.-H. Nguyen, R. Selvasembian, P. Singh, Recent advances on water disinfection using bismuth based modified photocatalysts: strategies and challenges, J. Clean. Prod. 297 (2021) 126617.
[27] G. Xu, M. Du, T. Li, Y. Guan, C. Guo, Facile synthesis of magnetically retrievable Fe_3O_4/$BiVO_4$/CdS heterojunction composite for enhanced photocatalytic degradation of tetracycline under visible light, Sep. Purif. Technol. 275 (2021) 119157.
[28] Y. Jin, Y. Shi, Z. Chen, R. Chen, X. Chen, X.i. Zheng, Y. Liu, R. Ding, Enhancement of solar water disinfection using H_2O_2 generated in situ by electrochemical reduction, Appl. Catal. B-Environ. 267 (2020) 118730.
[29] J. He, Z. Zheng, I.M.C. Lo, Different responses of gram-negative and gram-positive bacteria to photocatalytic disinfection using solar-light-driven magnetic TiO_2-based material, and disinfection of real sewage, Water Res. 207 (2021) 117816.
[30] J. Zhang, P. Su, H. Chen, M. Qiao, B. Yang, X.u. Zhao, Impact of reactive oxygen species on cell activity and structural integrity of Gram-positive and Gram-negative bacteria in electrochemical disinfection system, Sep. Purif. Technol. 451 (2023) 138879.
[31] W. Wang, H. Wang, G. Li, P.K. Wong, T. An, Visible light activation of persulfate by magnetic hydrochar for bacterial inactivation: efficiency, recyclability and mechanisms, Water Res. 176 (2020) 115746.
[32] Y. Yan, X. Zhou, P. Yu, Z. Li, T. Zheng, Characteristics, mechanisms and bacteria behavior of photocatalysis with a solid Z-scheme Ag/AgBr/g-C_3N_4 nanosheet in water disinfection, Appl. Catal. A-Gen. 590 (2020) 117282.
[33] Y. Li, J. Zhao, G. Zhang, L. Zhang, S. Ding, E. Shang, X. Xia, Visible-light-driven photocatalytic disinfection mechanism of Pb-$BiFeO_3$/rGO photocatalyst, Water Res. 161 (2019) 251–261.
[34] R. Wang, T. Wang, G. Qu, Y. Zhang, X. Guo, H. Jia, L. Zhu, Insights into the underlying mechanisms for integrated inactivation of A. spiroides and depression of disinfection byproducts by plasma oxidation, Water Res. 196 (2021) 117027.
[35] S. Kang, M. Herzberg, D. Rodrigues, M. Elimelech, Antibacterial effects of carbon nanotubes: size does matter!, Langmuir 24 (2008) 6409–6413.
[36] J. Monrás, B. Collao, R. Molina-Quiroz, G. Pradenas, L. Saona, V. Durán-Toro, N. Órdenes-Aenishanslins, F. Venegas, D. Loyola, D. Bravo, P. Calderón, I. Calderón, C. Vásquez, T. Chasteen, D. Lopez, J. Pérez-Donoso, Microarray analysis of the Escherichia coli response to CdTe-GSH Quantum Dots: understanding the bacterial toxicity of semiconductor nanoparticles, BMC Genomics 15 (2014) 1099.